Journal of Materials Research and Technology 30 (2024) 4961–4972

Contents lists available at ScienceDirect

Journal of Materials Research and Technology

journal homepage: www.elsevier.com/locate/jmrt

Hot deformation behavior and microstructure evolution of the Cu-1.5Ti-(0.5Fe) alloys

Gang'ao Xin [a], Meng Zhou [a,**], Ke Jing [a], Haoyan Hu [a], Zheng'ao Li [a], Yi Zhang [a,*], Caijiao Tian [a], Yonghui Sun [b], Baohong Tian [a], Xu Li [c], Alex A. Volinsky [d], Jin Zou [e,***]

[a] School of Materials Science and Engineering, Henan University of Science and Technology, Provincial and Ministerial Co-construction of Collaborative Innovation Center for Non-ferrous Metals New Materials and Advanced Processing Technology, Luoyang, 471023, China
[b] Chinalco Luoyang Copper Processing Co., Ltd., Luoyang, 471000, China
[c] Center for Advanced Measurement Science, National Institute of Metrology, Beijing, 100029, China
[d] Department of Mechanical Engineering, University of South Florida, 4202 E. Fowler Ave. ENG 030, Tampa, FL, 33620, USA
[e] Jiangxi Key Laboratory for Advanced Copper and Tungsten Materials, Jiangxi Academic of Sciences, Nanchang, 330096, China

ARTICLE INFO

Handling editor: L Murr

Keywords:
Cu-Ti-Fe alloys
Flow stress
Precipitated phase
Constitutive equations
Microstructure evolution

ABSTRACT

Compression tests of the Cu-1.5Ti and Cu-1.5Ti-0.5Fe alloys were carried out using the Gleeble-1500D hot deformation simulator. The deformation temperature was 750–900 °C and the strain rate was 0.1–0.003 s^{-1}. The Cu-1.5Ti-0.5Fe alloy clearly shows higher rheological stress and displays dynamic recovery and dynamic recrystallization characteristics under the same deformation conditions. The constitutive equations of the alloys were established. The activation energy of the Cu-1.5Ti alloy was 341.76 kJ/mol, which increased to 378.03 kJ/mol with the addition of 0.5 wt% Fe. After 750 °C and 0.003 s^{-1} deformation the Cu_4Ti phase precipitated in Cu-1.5Ti alloy. Adding 0.5 wt% Fe caused dynamic recrystallization during hot deformation. The hot-deformed Cu-1.5Ti-0.5Fe alloy had more dislocations and finer grains with Cu_4Ti and Fe_2Ti precipitated phases.

1. Introduction

Copper alloys have excellent properties, including high strength, electrical conductivity and corrosion resistance, and are widely used in modern industrial systems [1–3]. For instance, integrated circuits, advanced communications, high-speed rail transportation, and other industries need strong copper alloys with high electrical conductivity [4–6]. It is common to improve copper alloys' properties by adding different solute elements. Solute elements cause different types of phases to precipitate in the copper matrix, which can greatly improve the alloy performance. This precipitation strengthening mechanism has been recognized by a large number of scholars [7–9]. Typical precipitation-strengthened copper alloys include Cu-Ti [10,11], Cu-Ni-Si [12–14], Cu-Cr-Zr [15–17], etc. Cu–Ti alloys with excellent properties (high strength, high elasticity, and fatigue resistance) have gradually replaced toxic Cu–Be alloys in recent years [18].

It is believed that the precipitated β′ Cu_4Ti phase is the reason for the high strength of the Cu–Ti alloy. Huang et al. studied the Cu–3Ti–1Cr alloy and found that the precipitated β' Cu_4Ti phase is the main reason for high alloy strength due to precipitation strengthening [19]. Li et al. studied the aging process of the Cu-2.7Ti-0.15Mg-0.1Ce-0.1Zr alloy and found that the Cu_4Ti precipitated phase can effectively pin dislocations caused by cold rolling and improve the alloy strength [20]. However, Ti atoms that fail to precipitate in Cu–Ti alloys will scatter a large number of electrons, resulting in lower electrical conductivity. Therefore, adding new solute atoms to promote different types of precipitation is important to improve the properties of Cu–Ti alloys. Rouxel et al. found that after adding 0.3 wt% Fe to the Cu–6Ti, the yield strength of the solid solution alloy decreased from 521 MPa to 323 MPa, while the elongation reached 48%, and the formability was greatly improved [21]. Some scholars have found that Ti and Fe atoms can form a Fe_2Ti precipitated phase, which can inhibit the growth of recrystallized grains, refine grains, and improve alloy strength and high-temperature mechanical properties [22–24].

Mg, Ni, Sn and other elements are commonly added to Cu–Ti alloys. Li et al. found that the Cu_2Mg phase precipitated during the Cu–3Ti–2Mg

---

[*] Corresponding author.
[**] Corresponding author.
[***] Corresponding author.

E-mail addresses: zhoumeng0902@126.com (M. Zhou), zhshgu436@163.com (Y. Zhang), niatzou@126.com (J. Zou).

https://doi.org/10.1016/j.jmrt.2024.04.208
Received 25 March 2024; Received in revised form 23 April 2024; Accepted 24 April 2024

alloy aging, which helped to improve its hardness [25]. Liu et al. observed the Ni_3Ti precipitated phase in the aged Cu–3Ti–3Ni-0.5Si alloy, which improved the alloy properties [26]. Lebreton et al. added different amounts of Sn to the Cu–3Ti alloy to form $CuTi_3Sn_5$ eutectic compounds that could not be eliminated by heat treatment [27]. Wang et al. found $CuSn_3Ti_5$ compounds in the Cu–3Ti–2Sn alloys, and the lower solute atom content in the matrix improved the alloy electrical conductivity [28]. In summary, the Cu–Ti–Fe alloys show strong advantages in terms of performance and cost.

Hot working is used for industrial production of metals, and is the key to improving the microstructure of alloys [29,30]. Dynamic recrystallization is the main softening mechanism in hot deformation processing of copper alloys. Regulating dynamic recrystallization is a new way to improve the alloy properties [31–33]. Wang et al. found that the Cu-3.5Ti-0.2Fe alloy is more prone to dynamic recrystallization at high temperatures and low strain rates [34]. Zhao et al. studied hot deformation of Cu–15Ni–8Sn alloy and found that the precipitated phase particles nail the grain boundaries and inhibit recrystallized grain growth [35]. Current research focuses on the Cu–Ti alloys with medium and high Ti content, while there are a few studies of copper alloys with low Ti content. Hot deformation behavior of the Cu-1.5Ti and Cu-1.5Ti-0.5Fe alloys is studied in this paper, providing theoretical support for their industrial production.

2. Materials and experimental procedures

The raw materials to cast Cu-1.5Ti and Cu-1.5Ti-0.5Fe alloys with desired composition were high-purity electrolytic copper blocks (>99.99 wt%), Cu-10% Fe master alloy and high-purity titanium sponge particles (>99.45 wt%). The ZG-5Kg vacuum induction melting furnace was used for smelting alloys, and argon gas was introduced for protection during the melting process to prevent oxidation and inclusions in the alloy. After the alloy was melted, the composition of the middle sample area was measured by the Optima 2100 DV inductively coupled plasma atomic emission spectrometer, and the results are listed in Table 1. The alloy measured composition is basically the same as the designed composition.

Alloy ingots were electrical discharge machined (EDM), and cylindrical specimens with Φ8 mm × 12 mm dimensions were prepared for compression testing. In order to ensure the uniformity of the specimen composition, the sampling area was located in the middle of the ingot. Cylindrical specimens with smooth surfaces and no defects should be selected. In order to prevent cracks on the surface of the specimen due to stress concentration during hot compression, which affect the data accuracy, the cylindrical specimen surface was polished with 400–2000 mesh sandpaper, making sure that the upper and lower bottom surfaces of the cylinder were parallel.

Fig. 1(a) shows the alloy temperature processing history. Polished specimens were first solution treated in the OTF-1200X vacuum tube furnace at 920 °C for 60 min, after which they were quickly water-cooled to retain the solid solution structure. Argon gas was introduced into the furnace during the solution treatment process to prevent sample oxidation. The Gleeble-1500D numerical control dynamic thermo-mechanical simulation testing machine was used for compression tests. Combined with the Cu–Ti phase diagram and previous research results, selected temperatures for the compression tests were 750 °C, 800 °C, 850 °C, and 900 °C, and the strain rates were 1 s^{-1}, 0.1 s^{-1}, 0.01 s^{-1}, and 0.003 s^{-1}. The specimens were first heated to the target temperature at a 10 °C/s rate and held for 3 min, which ensured a uniform temperature distribution. Rapid water quenching after hot deformation was performed to preserve the sample high-temperature microstructure.

Table 1
Measured alloy chemical composition in wt.%.

Alloy	Cu	Ti	Fe
Cu-1.5Ti	Bal.	1.5	None
Cu-1.5Ti-0.5Fe	Bal.	1.52	0.5

Fig. 1(b) shows the testing flow chart. In order to study the evolution of the internal structure of the alloy after hot deformation, the deformed specimen was cut in the middle by EDM, and the cross-sectional structure was observed with an optical microscope. Electron backscatter diffraction (EBSD) and transmission electron microscopy (TEM) analysis was performed using JSM-7800F field emission scanning electron microscope and LIBRA-200FE transmission electron microscope, respectively. The preparation of EBSD specimens included grinding with 400–2000 mesh sandpaper, mechanical polishing, electrolytic polishing and other steps. The composition of the electropolishing electrolyte was a 1:1 mixture of phosphoric acid and alcohol solution. The power supply was MS-305D operated at 5 V for 60 s electropolishing. The electropolishing process was carried out entirely on a magnetic stirrer, which is the key to EBSD specimen preparation. TEM specimens were prepared using mechanical grinding and ion thinning.

3. Results

3.1. Flow stress

During hot deformation, externally applied loads generate stresses in the alloy, which deforms. Both stresses and stains are captured by the stress-strain curves. The internal structure of the alloy is affected by work hardening, dynamic recovery and dynamic recrystallization. Therefore, the true stress-strain curves dynamically reflect the evolution of the alloy internal structure, which is an important way to study alloy's properties.

Both alloys have a rapid rise in stress at the beginning of deformation in Fig. 2. A large number of dislocations are produced at this stage inside the alloy under the action of externally applied load, and dislocations are constantly entangled when moving. The alloy hardness increases rapidly due to work hardening. Fig. 2(a) shows true stress-strain curves of the two alloys deformed at different temperatures and 0.1 s^{-1} strain rate. Taking Cu-1.5Ti-0.5Fe alloy as an example, when the deformation temperature is 750 °C and 800 °C, the stress rapidly rises first, and then remains constant. However, when the deformation temperature is 850 °C and 900 °C, the stress shows a downward trend after rapidly rising to the highest point.

This is because the stress rises rapidly due to work hardening at the early deformation stage. Point defects migrate at higher strain, and dislocations get redistributed, resulting in dynamic recovery of the alloy. The combination of work hardening and recovery keep the true stress unchanged after reaching the maximum. When the deformation temperature is increased further, the distortion-free crystal nuclei will continue to form and grow in the high distortion energy regions caused by the alloy deformation, which consumes the energy stored in the form of dislocations, decreasing the true stress. The work hardening and recrystallization reach a balance, and the dislocations are continuously generated and consumed, so that the true stress rises to the peak value and then decreases. Dynamic recrystallization occurs in this process.

Fig. 2(a, b, d) shows the true stress-strain curves of the alloys deformed at different strain rates. The flow stress of the two alloys decreases with deformation temperature for the same strain rate. This is because the atomic diffusion rate is faster at higher deformation temperatures, recovery and recrystallization are more likely to occur, the distortion energy inside the alloy is continuously released, and the stress is reduced. For the same deformation temperature, the flow stress increases with the strain rate in Fig. 2(e). This is because when the deformation rate increases, a large number of dislocations accumulate inside the alloy in a short period of time, and the internal distortion energy stored in the form of dislocations cannot be released in time, the dynamic softening effect is reduced, and the stress is continuously increased. The Fe addition changes the curves' characteristics in Fig. 2 (a, b, d, e), and the Cu-1.5Ti alloy exhibits work hardening

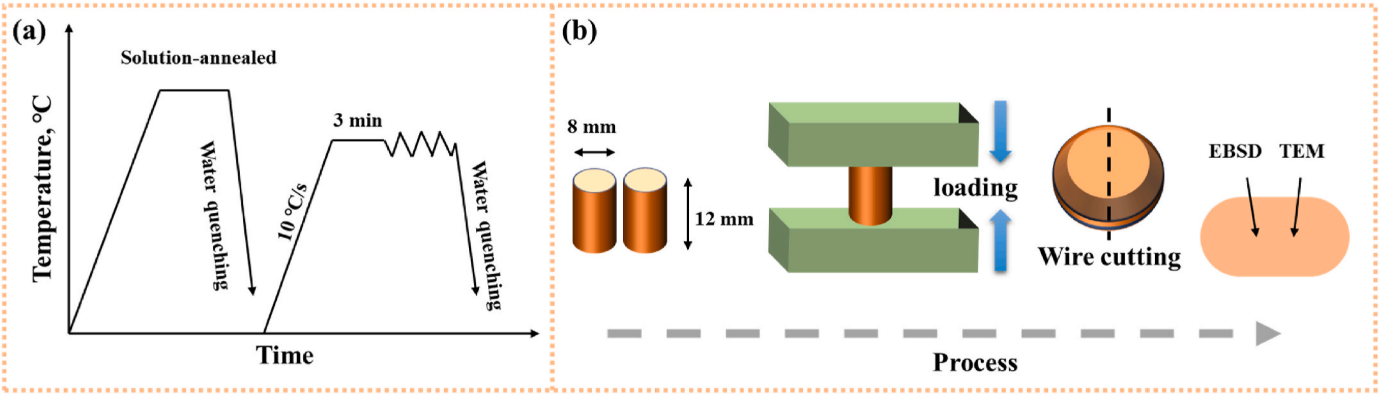

Fig. 1. (a) Alloy temperature processing history; (b) Testing flow chart.

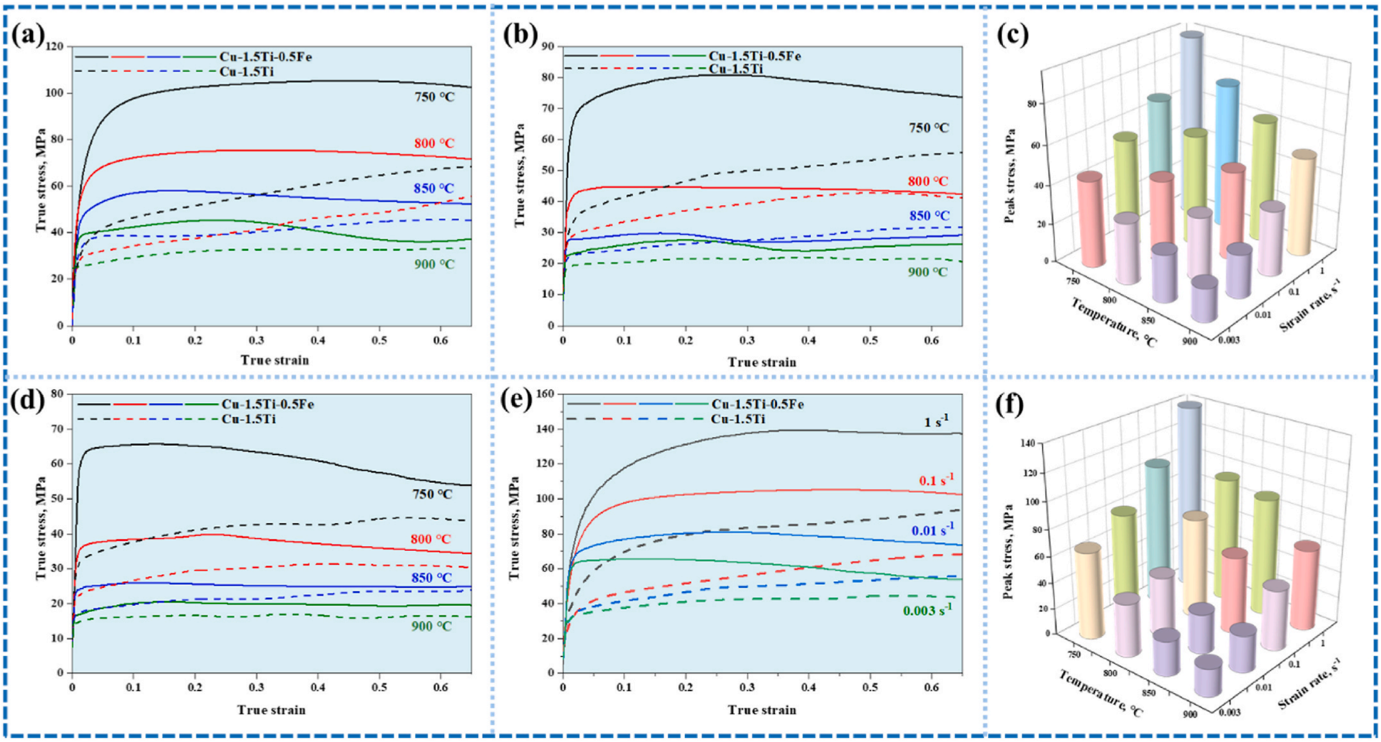

Fig. 2. True stress-strain curves and peak stresses of the Cu-1.5Ti and Cu-1.5Ti-0.5Fe alloys deformed at different conditions: (a) 0.1 s^{-1}; (b) 0.01 s^{-1}; (c) Peak stress of the Cu-1.5Ti alloy; (d) 0.003 s^{-1}; (e) 750 °C; (f) Peak stress of the Cu-1.5Ti-0.5Fe alloy.

characteristics, while the Cu-1.5Ti-0.5Fe alloy mainly exhibits dynamic recovery and dynamic recrystallization.

Fig. 2(c–f) shows the peak stresses of the two alloys under different deformation conditions, and the peak flow stresses are maximized when the two alloys were deformed at 750 °C and 1 s^{-1}. When the thermal deformation parameters are 900 °C and 0.003 s^{-1}, the peak flow stress of the two alloys is minimized. Combined with the true stress-strain curves of the alloy, one can conclude that the high deformation temperature and low strain rate contribute to the dynamic recrystallization processes. When the strain rate is 0.1 s^{-1} and the deformation temperature is 750 °C, 800 °C, 850 °C and 900 °C, the peak stresses of the Cu-1.5Ti alloy are 68.4 MPa, 56.8 MPa, 45.6 MPa, and 33.5 MPa, respectively, while the peak stresses of the Cu-1.5Ti-0.5Fe alloy are 105.3 MPa, 75.5 MPa, 58.1 MPa, and 45.4 MPa, respectively. This indicates that the Fe addition can significantly increase the flow stress of the alloy, which is related to different precipitated phases.

3.2. Constitutive equations

The plastic deformation of alloys is accompanied by the movement of atoms, and the energy barrier that needs to be crossed to drive the motion of atoms can be represented by thermal deformation activation energy. According to the model proposed by Sellaes and McTegart [36], the relationship between hot deformation temperature, strain rate, and flow stress can be described as:

$$\dot{\varepsilon} = A \cdot \sinh\,(\alpha\sigma)^{n}\exp\left(-\frac{Q}{RT}\right)\ (\mathrm{All}) \tag{1}$$

$$\dot{\varepsilon} = A_1\sigma^{n_1}\exp\left(-\frac{Q}{RT}\right)\ (\alpha\sigma < 0.8) \tag{2}$$

$$\dot{\varepsilon} = A_2\exp\left(\beta\sigma - \frac{Q}{RT}\right)\ (\alpha\sigma > 1.2) \tag{3}$$

Taking natural logarithms of both sides of equations (1)–(3) yields:

$$\ln\dot{\varepsilon} = n\ \ln[\sinh(\alpha\sigma)] - \frac{Q}{RT} + \ln A \tag{4}$$

$$\ln\dot{\varepsilon} = n_1\ \ln\sigma + \ln A_1 - \frac{Q}{RT} \tag{5}$$

$$\ln\dot{\varepsilon} = \beta\sigma + \ln A_2 - \frac{Q}{RT} \tag{6}$$

Here, $\dot{\varepsilon}$ is the strain rate in s^{-1}; Q is the activation energy of hot deformation in KJ/mol; σ is the peak stress of the alloy deformation process in MPa; R is constant, and the value is 8.314 J/(mol·K); T is the alloy deformation temperature in K; and A, A_1, A_2, n, n_1, β, $\alpha = \beta/\ n_1$ are constants.

The activation energy Q for thermal deformation of an alloy is an important parameter [37]. Taking partial derivative of Eq. (1) with respect to T yields the formula for calculating Q:

$$Q = R\left[\frac{\partial(\ln\dot{\varepsilon})}{\partial\ln[\sin\ \alpha\sigma]}\right]_T \left[\frac{\partial\ln[\sinh(\alpha\sigma)]}{\partial(1/T)}\right] = RNS \tag{7}$$

A large number of studies have shown that there is the following relationship between lattice self-diffusion energy Z, stress and temperature [38,39]:

$$Z = \dot{\varepsilon}\exp\left(\frac{Q}{RT}\right) \tag{8}$$

Substituting Eq. (8) into Eq. (1), and taking natural logarithm yields:

$$\ln Z = \ln A + n\ \ln[\sinh(\alpha\sigma)] \tag{9}$$

Fig. 3 shows parameters for calculating the constitutive equation of the Cu-1.5Ti-0.5Fe alloy. $1/\beta$, $1/n_1$, $1/N$, S, and n correspond to the average slopes of the straight lines in Fig. 3(a–e), respectively, so $\beta = 0.103$, $n_1 = 6.012$, $N = 4.297$, $S = 10.582$, and $n = 4.158$. The intercepts in Fig. 3(e) are represented by $lnA = 37.7$, $A = 2.36 \times 10^{16}$.

The constitutive equation of the Cu-1.5Ti-0.5Fe alloy is:

$$\dot{\varepsilon} = 2.36 \times 10^{16}[\sinh(0.017\sigma)]^{4.16}\exp\left(-\frac{378,033}{RT}\right) \tag{10}$$

Using the same method, the constitutive equation for the Cu-1.5Ti alloy is obtained as:

$$\dot{\varepsilon} = 4.28 \times 10^{14}[\sinh(0.022\sigma)]^{4.86}\exp\left(-\frac{341,757}{RT}\right) \tag{11}$$

Fig. 3(f) shows the activation energy of thermal deformation for the two alloys. The Cu-1.5Ti-0.5Fe alloy has higher thermal deformation activation energy of 378.033 kJ/mol, compared to 341.76 kJ/mol for the Cu-1.5Ti alloy. The thermal deformation activation energy increases by 10.6% after adding Fe, indicating that the alloy's ability to resist thermal deformation is significantly improved. This is related to the fact that the addition of Fe promotes precipitation of secondary phases, thereby hindering the dislocation movement during thermal deformation, which is analyzed in detail in the discussion section.

3.3. *Microstructure evolution*

The changes in the true stress-strain curves and the difference in the activation energy of thermal deformation are closely related to the internal microstructure of the alloy. In order to study the microstructure changes of the alloy during thermal deformation under different parameters, metallographic observations were carried out in the middle section of the samples after deformation was completed. Fig. 4 shows the microstructure of the two alloys deformed at different temperatures and 0.003 s^{-1} strain rate. In Fig. 4(a) the grains of the Cu-1.5Ti-0.5Fe alloy are significantly elongated, and the grain elongation is perpendicular to the compression direction. At 750 °C deformation temperature the alloy is composed of deformed grains and a small amount of recrystallized grains. At higher temperature a large number of fine dynamic recrystallization (DRX) grains are produced in Fig. 4(b).

This is because during the deformation process, the dislocations

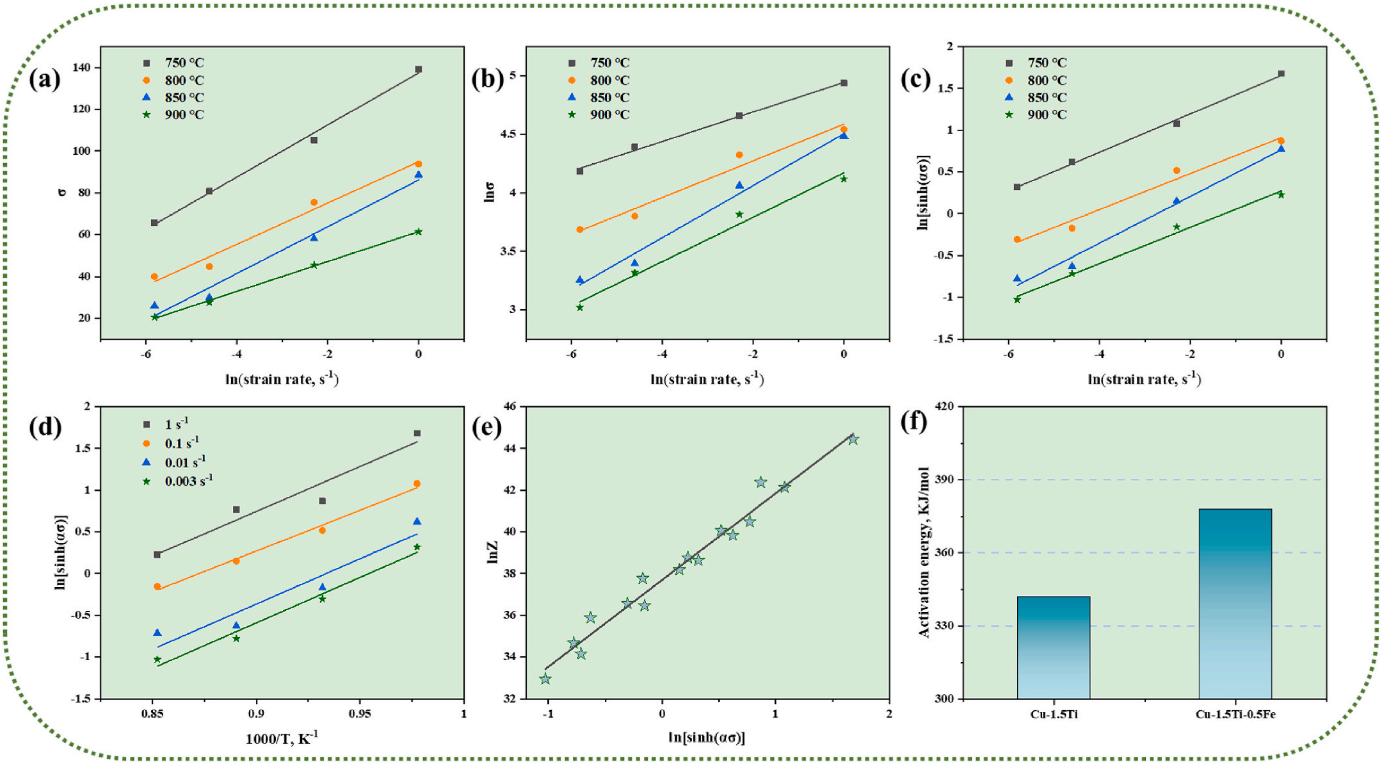

Fig. 3. (a–e) Parameters of the Cu-1.5Ti-0.5Fe alloy; (f) Activation energy of the Cu-1.5Ti and Cu-1.5Ti-0.5Fe alloys.

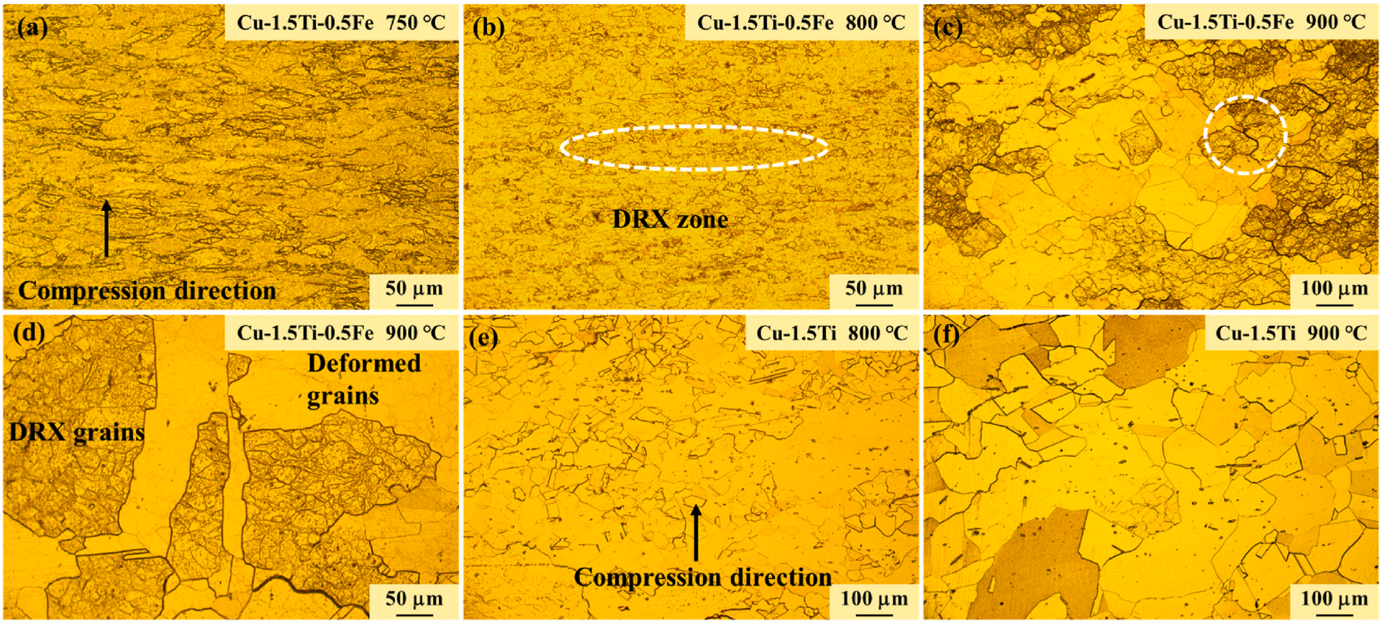

Fig. 4. Microstructure of the Cu-1.5Ti and Cu-1.5Ti-0.5Fe alloys deformed at 0.003 s^{-1} strain rate and (a) 750 °C; (b, e) 800 °C; (c, d, f) 900 °C.

moving inside the alloy are easily hindered by grain boundaries and continue to entangle and aggregate to form bands. With the increase of deformation temperature, the dynamic recrystallization process is preferentially started in the deformation region with high energy, and dislocation energy is an important driving force for dynamic recrystallization. As seen in Fig. 4(c and d), as the deformation temperature increases to 900 °C, the recrystallized grains grow sufficiently and the number of recrystallized grains increases significantly. At higher temperatures, the DRX region indicated by the white dotted circle in Fig. 4 (c) increases because the high temperature accelerates the movement of grain boundaries and contributes to the growth of recrystallized grains. It is evident from Fig. 4(d) that there are both fine equiaxed grains with DRX and deformed grains without DRX. As seen in Fig. 4(e and f), the Cu-1.5Ti alloy is similar to the Cu-1.5Ti-0.5Fe alloy. The grain size of the Cu-1.5Ti alloy increased significantly with deformation temperature. Under the same thermal deformation conditions, the Cu-1.5Ti-0.5Fe alloy has smaller grains, which indicates that the Fe addition plays a role in inhibiting the grain growth.

3.4. EBSD analysis

In order to conduct a more in-depth analysis of the alloy microstructure after hot deformation and explore the influence of different temperatures on the evolution of the alloy macrostructure, EBSD analysis was performed. Fig. 5 shows the EBSD plot and grain size of the alloys deformed at 0.003 s^{-1} strain rate. Fig. 5(a–c) shows the Cu-1.5Ti-0.5Fe alloy deformed at 750 °C, 800 °C and 900 °C. As seen in Fig. 5(a), at 750 °C deformation temperature, a large number of grains are significantly elongated, showing the characteristics of deformed grains, and many fine recrystallized grains appear in the alloy. The average grain size of the sample was 13.26 μm, and the grains less than 15 μm accounted for 69.1%. In Fig. 5(b), the recrystallized grains are significantly larger as the deformation temperature increased to 800 °C, but the average grain size is 13.27 μm, which is not significantly larger than in Fig. 5(a).

This is because in the dynamic recrystallization process, when the temperature increases, the growth rate and nucleation rate of the recrystallized grains increase at the same time, which slightly changes the overall grain size. At this time, the grains less than 15 μm accounted for 72.2% of the grains, and the proportion of small grains was further increased, which means that the higher temperature increased the degree of recrystallization of the alloy. As seen in Fig. 5(c), when the deformation temperature reached 900 °C, the recrystallized grains have fully grown, with 171.32 μm average size, and 83.3% of the grains larger than 60 μm. Fig. 5(d) shows the microstructure of the Cu-1.5Ti alloy after 800 °C deformation, with an average grain size of 74.38 μm. It can be seen in Fig. 5(b) that under the same deformation conditions, the alloy grains are significantly smaller after the addition of Fe. This indicates that Fe can inhibit the grain growth during dynamic recrystallization and plays a role in grain refinement. This is also an important reason why Cu-1.5Ti-0.5Fe alloy has higher flow stress.

During the thermal deformation of the metal, the deformation causes accumulation of dislocations in the internal structure of the alloy. At the same time, the dynamic recovery and dynamic recrystallization processes continuously release internal distortion energy, consume dislocations, and form a dynamic equilibrium. Therefore, the dislocation density can reflect the dynamic recrystallization of the alloy to a certain extent. Fig. (6) shows the Kernel average misorientation (KAM) and grain orientation spread (GOS) plots of the alloy for the 0.003 s^{-1} strain rate. In the KAM diagram, red represents high dislocation density, and blue represents low dislocation density. The color scale on the right side of the GOS plot shows the GOS value of the grain. Fig. 6(a–c) and (e-g) show Cu-1.5Ti-0.5Fe alloy deformed at 750 °C, 800 °C and 900 °C, respectively. It can be seen from the KAM diagram in Fig. 6(a–c) that with the continuous increase of deformation temperature, the dislocation density shows a significant downward trend. The geometrically necessary dislocation density can be calculated as in Ref. [40]:

$$\rho = 2\theta / \mu b \tag{12}$$

Here, ρ represents the density of geometrically necessary dislocations in m^{-2}, and θ is the average local misorientation in rad, b the Burgers vector of the alloy of 0.255 nm, and μ is the scanning step size of EBSD in μm. Calculations show that the geometrically necessary dislocation density of the Cu-1.5Ti-0.5Fe alloy deformed at 750 °C is $\rho = 2.72 \times 10^{14}$ m^{-2}, at 800 °C $\rho = 1.85 \times 10^{14}$ m^{-2}, and at 900 °C $\rho = 7.28 \times 10^{13}$ m^{-2}. The continuous decrease in dislocation density indicates that in the process of hot deformation, higher temperatures increase the nucleation rate and the growth rate of dynamically recrystallized grains, accelerating the release of stored energy within the alloy, thereby maintaining the dislocation density of the structure at a lower level.

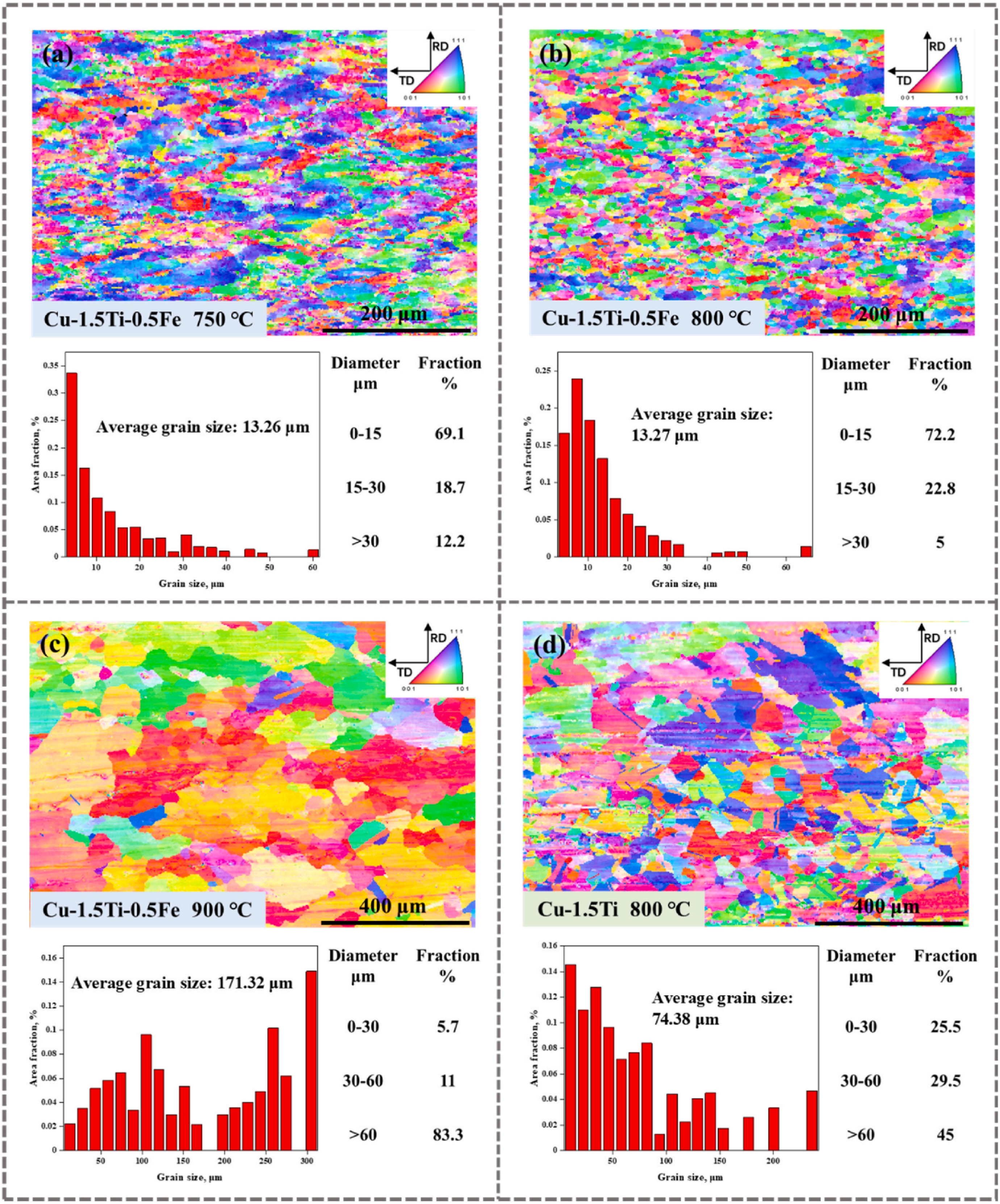

Fig. 5. EBSD plot and grain size of the alloy longitudinal section deformed at 0.003 s^{-1} strain rate: (a) Cu-1.5Ti-0.5Fe alloy deformed at 750 °C; (b) Cu-1.5Ti-0.5Fe alloy deformed at 800 °C; (c) Cu-1.5Ti-0.5Fe alloy deformed at 900 °C; (d) Cu-1.5Ti alloy deformed at 800 °C.

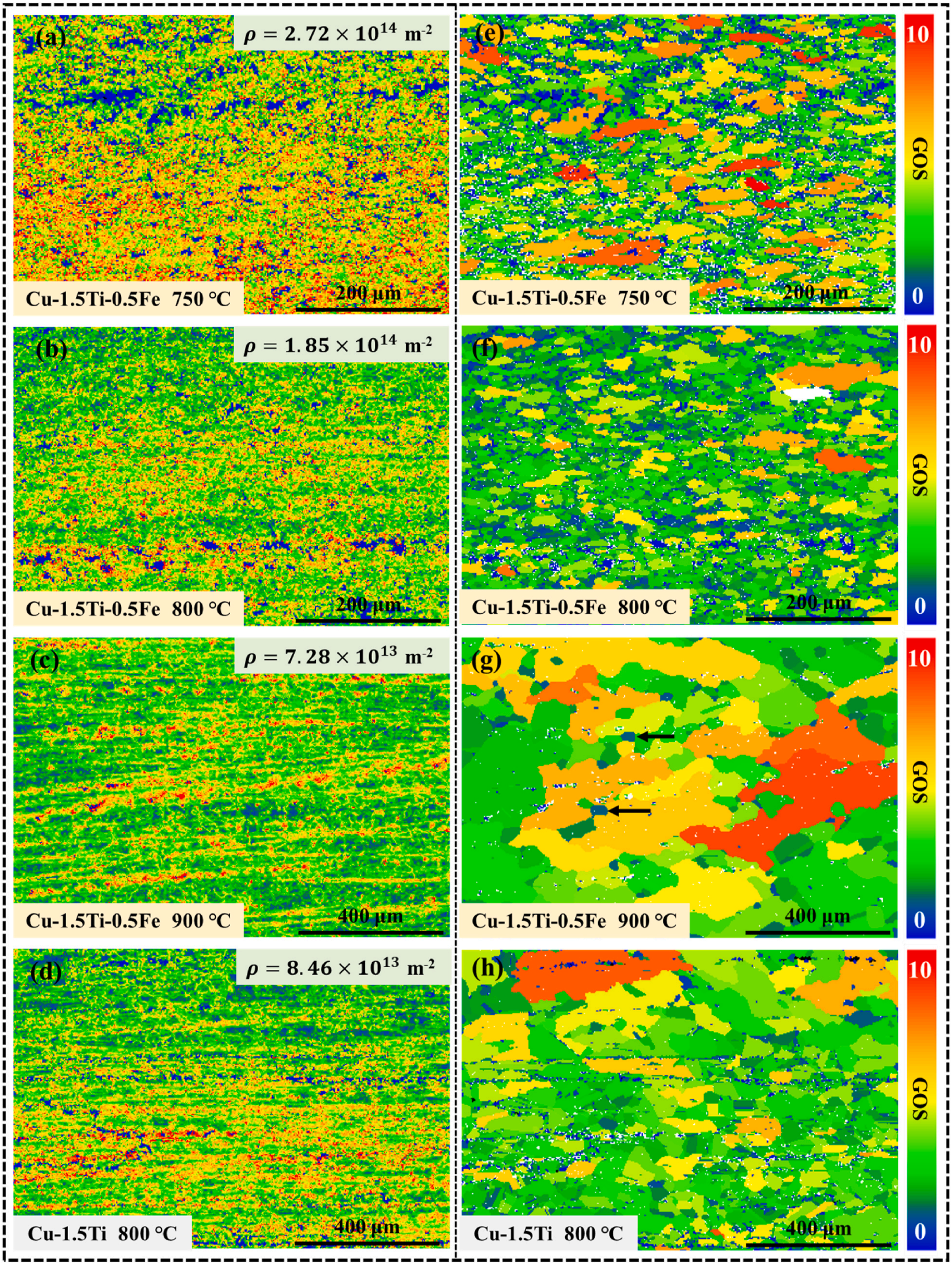

Fig. 6. Kernel average misorientation and grain orientation spread plots of the longitudinal section structure of the alloys deformed at 0.003 s^{-1} strain rate: (a, e) Cu-1.5Ti-0.5Fe alloy deformed at 750 °C; (b, f) Cu-1.5Ti-0.5Fe alloy deformed at 800 °C; (c, g) Cu-1.5Ti-0.5Fe alloy deformed at 900 °C; (d, h) Cu-1.5Ti alloy deformed at 800 °C.

The GOS map reflects the range of orientation distribution within the grains. The GOS value of the newly formed recrystallized grains is very small, generally defined as less than 2° for recrystallized grains [41–43]. As the grains deform, the value of GOS keeps increasing, forming deformed grains. It can be seen in the GOS graphs in Fig. 6(e–g) that as the hot deformation temperature rises from 750 °C to 800 °C, the number of deformed grains in the structure significantly decreases, further enhancing the degree of alloy recrystallization, which corresponds to lower dislocation density. It is clearly observed from Fig. 6(g) that recrystallized grains continue to grow but are also continuously compressed, forming red deformed grains. At the boundaries of these high-energy deformed grains, new recrystallized grains constantly form (as indicated by the black arrows), clearly showing the process of dynamic recrystallization. Fig. 6(d–h) shows the microstructure of the Cu-1.5Ti alloy after 800 °C deformation, with the dislocation density of $\rho = 8.46 \times 10^{13}$ m^{-2}. Compared with the Cu-1.5Ti alloy, the Cu-1.5Ti-0.5Fe alloy shown in Fig. 6(b–f) has a higher dislocation density and also a higher degree of recrystallization.

This study defines grains with grain orientation spread GOS<2° as small new DRX grains. By distinguishing alloy grains in the inverse pole figure (IPF) maps based on the GOS values, DRX grains (GOS<2°) and non-DRX grains (GOS ≥ 2°) are obtained in Fig. 7(a–f) for the Cu-1.5Ti-0.5Fe alloy and Fig. 7(g and h) for the Cu-1.5Ti alloy. It can be seen from Fig. 7(a–c, e) that with the increase in deformation temperature, the DRX grains of the Cu-1.5Ti-0.5Fe alloy increase in size. Combined with Table 2, one can see that at 750 °C, 800 °C, and 900 °C hot deformation, the average size of DRX grains is 4.42 μm, 6.68 μm, and 46.2 μm respectively. This is related to the fact that high temperatures accelerate the growth rate of dynamic recrystallization grains. It can be observed that the DRX grain size increases significantly as the temperature rises from 800 °C to 900 °C. This is because high temperatures reduce precipitation in the alloy, which weakens the resistance to grain boundary motion and promotes grain growth.

In the pole figures of Fig. 7, the color levels indicate different texture strengths, with red indicating the highest strengths. The pole figures in Fig. 7(a–c, e) show that the texture strength of DRX grains increases with

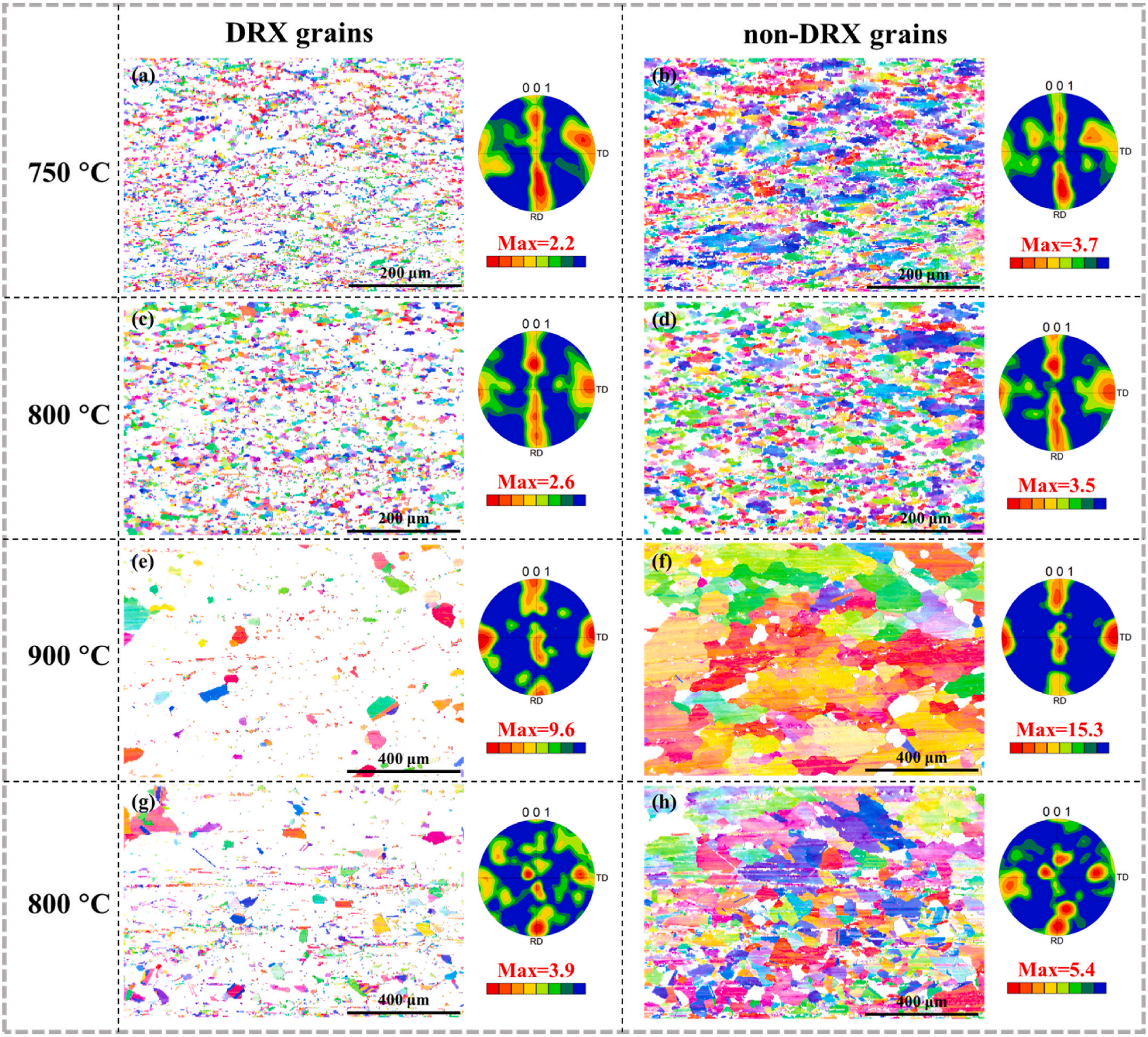

Fig. 7. Grain maps and pole figures of the longitudinal section of alloys deformed at 0.003 s^{-1} strain rate: (a–f) Cu-1.5Ti-0.5Fe alloy; (g, h) Cu-1.5Ti alloy.

Table 2
Volume fraction and grain size of DRX and non-DRX grains in heat-deformed tissues.

Alloys	Deformation temperature, °C	DRX grain fraction, %	DRX grain size, μm	Non-DRX grain size, μm
Cu-1.5Ti-0.5Fe	750	27.3	4.42	16.9
Cu-1.5Ti-0.5Fe	800	33.5	6.68	16.7
Cu-1.5Ti-0.5Fe	900	8.4	46.2	183
Cu-1.5Ti	800	16.1	25.6	84

deformation temperature. Comparison with standard pole figures revealed that the Cu-1.5Ti-0.5Fe alloy exhibited the {100}<001> Cube texture for DRX grains. A detailed analysis of Fig. 7(a–c, e) and Fig. 7(b–d, f) indicates that non-DRX grains are notably larger in size, have a higher proportion of grains, and exhibit stronger texture compared to DRX grains. Combined Table 2, one can see that at 750 °C, 800 °C, and 900 °C hot deformation, the average size of non-DRX grains is 16.9 μm, 16.7 μm, and 183 μm, respectively. Compared with DRX grains, non-DRX grains have higher texture strength, and there is no significant change in texture type. The microstructure and pole figures of the Cu-1.5Ti alloy after 800 °C deformation in Fig. 7(g and h) do not exhibit any dominant texture. The main texture types include {123}<634> S, {011}<100> Goss, and {100}<001> Cube textures.

The addition of Fe has significantly altered the texture type of the alloy's hot deformation structure. The DRX and non-DRX grain sizes of the Cu-1.5Ti alloy are 25.6 μm and 84 μm, respectively, in Table 2. Compared with the Cu-1.5Ti-0.5Fe alloy deformed at the same 800 °C temperature, the grains are significantly larger because Fe addition promotes the formation of more precipitated phases, which have a stronger pinning effect on grain boundaries. Further discussion of the specific content of the precipitate phases is provided later in the paper.

4. Discussion

4.1. Effect of Fe on the precipitated phases

During the thermal deformation of the alloy, supersaturated solute elements are continuously precipitated to form different types of precipitated phases. The dislocation slip will interact with the precipitated phase to form high-energy regions such as dislocation cells and dislocation walls, which are conducive to the generation of new crystal nuclei in the dynamic recrystallization process. By adjusting the thermal deformation parameters of the alloy, the size, number, and distribution of the precipitated phases can be changed, thereby controlling the dynamic recrystallization process and improving the alloy properties. Therefore, it is necessary to analyze the precipitated phases of the alloy after hot deformation. Fig. 8 shows TEM images and analysis of the Cu-1.5Ti alloy deformed at 750 °C and 0.003 s^{-1} strain rate. Fig. 8(a) is a brightfield image, where the deformation-induced dislocation structure of the alloy can be clearly seen. It can be observed from Fig. 8(b) that after the alloy is deformed, the internal dislocations are continuously entangled during the movement to form a dislocation wall structure. It can be observed from the HRTEM image in Fig. 8(c), that a precipitated phase is generated inside the alloy, which is the key to the change in alloy properties.

In order to determine the specific type of precipitated phase, the FFT transformation was performed in the white box area in Fig. 8(d) to obtain the diffraction spots shown in Fig. 8(e). After calibration, three crystal plane orientations of $(21\bar{3})_{Cu4Ti}$, $(02\bar{2})_{Cu4Ti}$ and $(\bar{2}11)_{Cu4Ti}$ were obtained, and the type of precipitated phase was determined to be Cu_4Ti. The IFFT transformation of the diffraction spots shown in Fig. 8(e) yields Fig. 8(f), where the plane spacing of the $(\bar{2}11)_{Cu4Ti}$ and $(21\bar{3})_{Cu4Ti}$ planes is calculated to be 0.2042 nm and 0.1815 nm, respectively. The fast Fourier transform of the white box area in Fig. 8(c) yields Fig. 8(g). After calibration, it is Cu with a ribbon axis of $[\bar{1}10]$ and crystal planes of $(111)_{Cu}$, $(11\bar{1})_{Cu}$ and $(00\bar{2})_{Cu}$. It can be seen from the IFFT plot of Cu in Fig. 8(h), that the spacing between the $(00\bar{2})_{Cu}$ and $(111)_{Cu}$ planes is 0.1833 nm and 0.2104 nm, respectively.

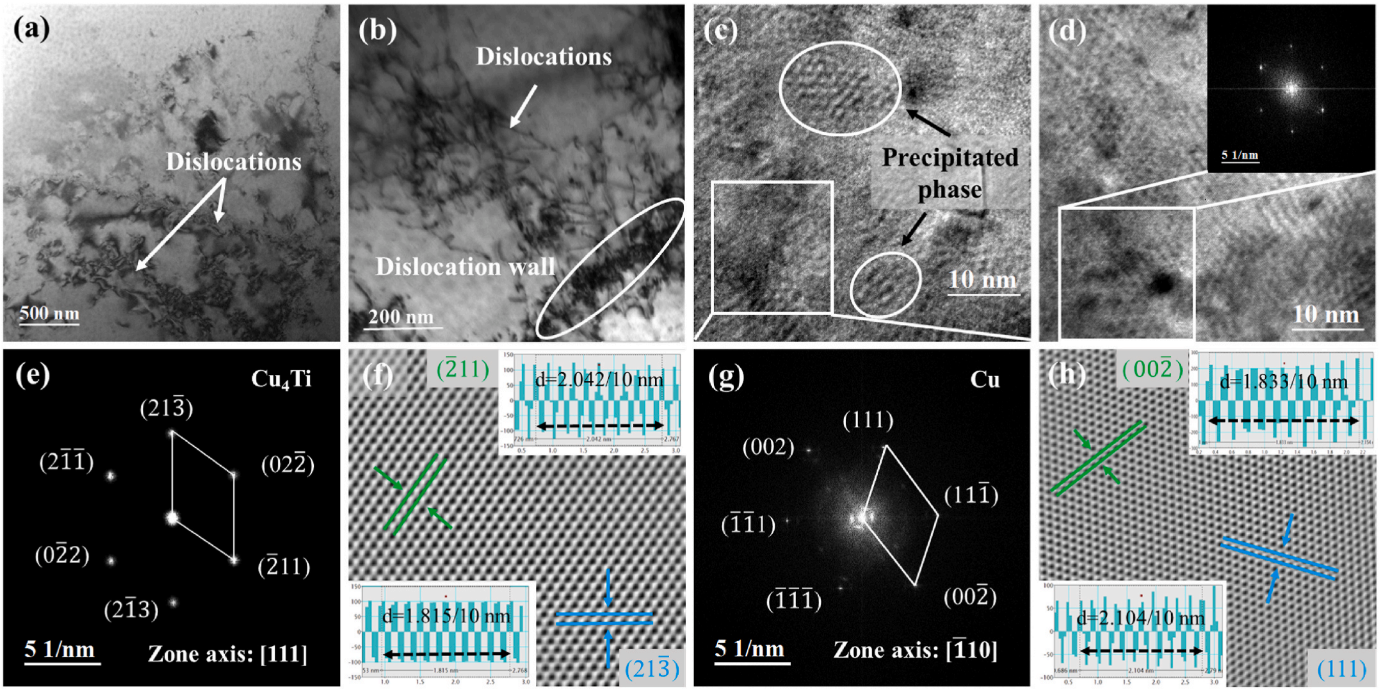

Fig. 8. TEM analysis of the Cu-1.5Ti alloy deformed at 750 °C and 0.003 s^{-1}: (a, b) Brightfield image; (c, d) HRTEM microstructure of alloys; (e) Fast Fourier transform (FFT) of Cu_4Ti; (f) Inverse FFT (IFFT) of Cu_4Ti; (g) FFT of Cu; (h) IFFT of Cu.

Fig. 9 shows TEM images and analysis of the Cu-1.5Ti-0.5Fe alloy deformed at 750 °C and 0.003 s^{-1}. There is a large number of dislocation structures inside the alloy in Fig. 9(a). Compared with the Cu-1.5Ti alloy, the Cu-1.5Ti-0.5Fe alloy has significantly higher dislocation density, which is consistent with the results in Fig. 6. This is because more precipitates have a stronger hindrance effect on dislocations with the addition of solute elements. Fig. 9(b) shows the cellular dislocation structure formed by the continuous entanglement of dislocations in motion. As seen in Fig. 9(c)–a large number of nanoscale precipitated phases are generated inside the alloy. The precipitated phase has ellipsoidal and long rod morphologies. In order to further determine the type of precipitated phase, selective area electron diffraction (SAED) was performed on precipitated phases of different shapes. Fig. 9(e) shows the brightfield images of the two types of precipitated phase particles, and the selective area electron diffraction spots of the long rod-shaped precipitated phase are shown in Fig. 9(d). After calibration, the precipitated phase was determined to be Cu_4Ti. Fig. 9(f) shows the selective electron diffraction spots of the ellipsoidal precipitated phase, which was calibrated to be Fe_2Ti.

In Fig. 9(e) the ellipsoidal precipitated phase is surrounded by dislocations at the edges with obvious traces of pinned dislocations. This further explains that the Cu-1.5Ti-0.5Fe alloy has a higher dislocation density and smaller grain size than the Cu-1.5Ti alloy under the same deformation conditions. Fig. 9(g) is a brightfield image of the ellipsoidal precipitated phase, where the HRTEM image of the white box area is shown in Fig. 9(h). Fig. 9(i) is the FFT plot of Fig. 9(h), and after calibration, it is Fe_2Ti with a band axis of [100]. The IFFT plot in Fig. 9(j) shows that the spacing of the $(010)_{Fe2Ti}$ and $(001)_{Fe2Ti}$ planes is 0.4284 nm and 0.8138 nm, respectively.

Previous research has found that aging treatment can significantly improve the comprehensive performance of Cu-1.5Ti-0.5Fe alloy, and precipitation strengthening mechanism is the main strengthening mechanism of the alloy. After aging treatment at 450 °C for 4 h, the main types of precipitated phases in Cu-1.5Ti-0.5Fe alloy are Cu_4Ti and Fe_2Ti [44]. The microstructure of the alloy after thermal deformation has the same types of precipitated phases as the aged microstructure, providing more comprehensive theoretical support for the evolution of the alloy's microstructure and changes in performance.

4.2. *Effect of Fe on dislocation density and grain size*

Hot deformation is an important way to improve the performance of metals. The DRX process can be controlled by changing hot deformation parameters such as temperature and strain rate, resulting in different grain sizes. Dislocations continue to accumulate during the deformation process, promoting generation of subgrain boundaries, which has a significant impact on the migration of grain boundaries during the DRX process.

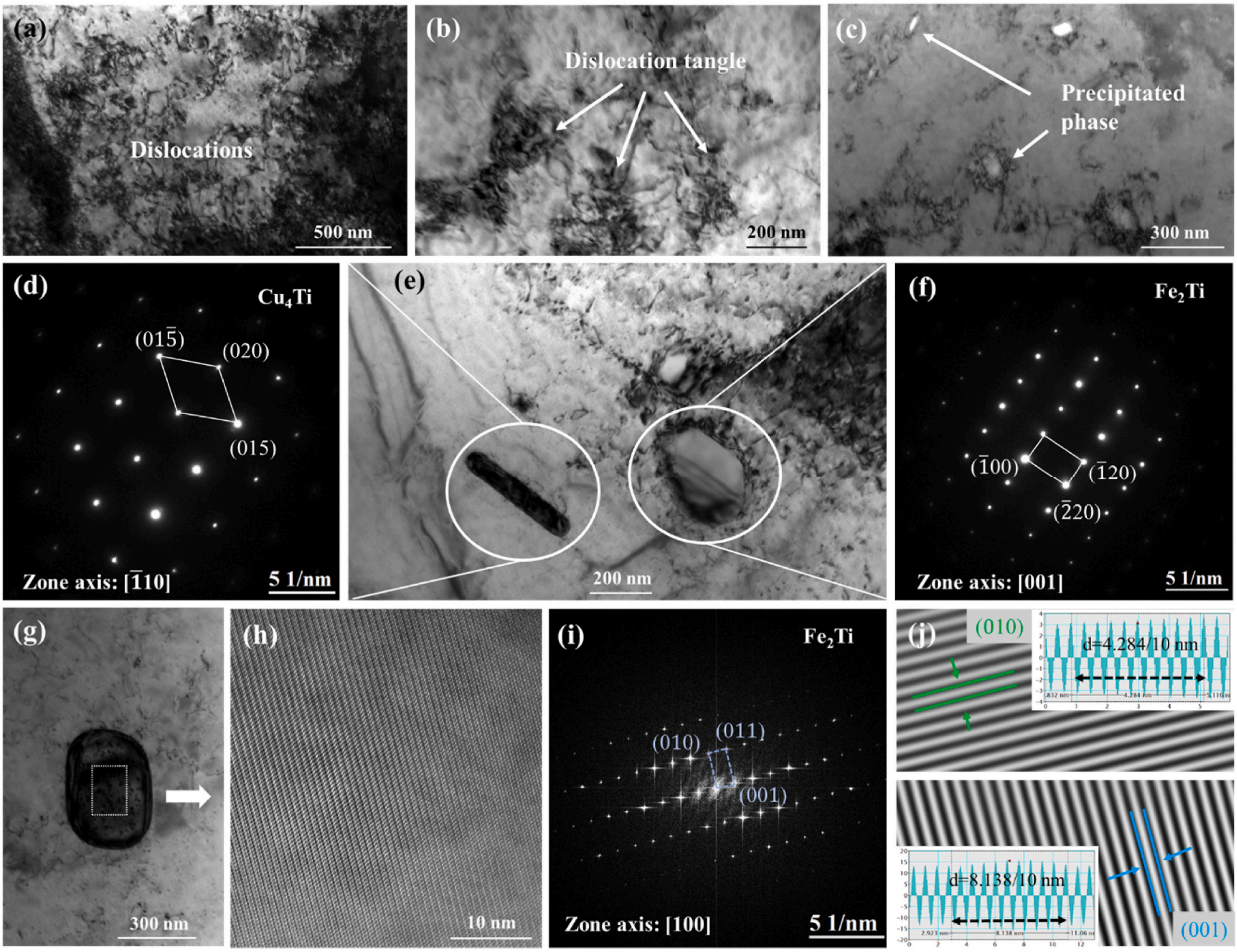

Fig. 9. TEM analysis of the Cu-1.5Ti-0.5Fe alloy deformed at 750 °C and 0.003 s^{-1}: (a–c) Brightfield images; (e) Brightfield image; (d, f) Diffraction spots of two precipitated phases; (g) Precipitated phase; (h) HRTEM of the precipitated phase in (g); (i) FFT of Fe_2Ti; (j) IFFT of Fe_2Ti.

To ensure the correctness and reproducibility of the experimental results, all analysis tests are conducted according to a uniform standard procedure. Prepare multiple hot deformation samples in the same state and conduct repeated experiments to ensure the reproducibility of the results. During the testing process, all obtained data are classified, labeled, and saved. For samples that require microscopic structure comparison, all conditions except the variable are kept consistent. Therefore, we can obtain the following more accurate analysis.

It can be seen from Fig. 6(b–d) that when deformed at 800 °C and 0.003 s^{-1}, the addition of 0.5 wt% Fe increases the geometrically necessary dislocation density of the Cu-1.5Ti alloy from $\rho = 8.46\times 10^{13}$ m^{-2} to $\rho = 1.85 \times 10^{14}$ m^{-2}, which is a significant increase. Higher dislocation density results in more energy stored within the alloy, which is continuously released as the grain boundaries migrate, promoting the DRX of the alloy. The true stress-strain curve in Fig. 2 shows that the Cu-1.5Ti-0.5Fe alloy mainly exhibits characteristics of dynamic recovery and dynamic recrystallization, which also confirms this viewpoint.

It can be seen from Fig. 5(b–d) that when deformed at 800 °C and 0.003 s^{-1}, the addition of 0.5 wt% Fe reduces the grain size of the Cu-1.5Ti alloy from 74.38 μm to 13.27 μm, which is an 82% decrease. This indicates that the addition of Fe can significantly refine the grain size of the Cu-1.5Ti alloy, which is related to the Fe_2Ti precipitation in the alloy. Grain refinement can effectively improve the strength and plasticity, making it possible for the Cu-1.5Ti-0.5Fe alloy to have excellent comprehensive performance.

5. Conclusions

This study investigated the hot deformation behavior of the Cu-1.5Ti and Cu-1.5Ti-0.5Fe alloys through isothermal hot compression tests at 750–900 °C and 0.1–0.003 s^{-1} strain rates. The main research findings are summarized as follows.

1. The flow stress is inversely proportional to the deformation temperature and directly proportional to the strain rate. Fe addition boosts Cu-1.5Ti-0.5Fe alloy’s flow stress. At 0.1 s^{-1} and 750 °C, 0.5 wt% Fe increases the Cu-1.5Ti peak stress from 68.4 MPa to 105.3 MPa.
2. Adding Fe promotes the transformation of the true stress-true strain curve of the alloy into dynamic recrystallization characteristics. By establishing the constitutive equation, the activation energy of Cu-1.5Ti alloy is 341.76 kJ/mol, while Cu-1.5Ti-0.5Fe is 378.03 kJ/mol, an increase of 10.6%.
3. After 800 °C deformation, the main textures of Cu-1.5Ti alloy were {123}<634>S and {011}<100>Goss, and the addition of Fe element transformed the alloy into {100}<001>Cube texture.
4. The Cu-1.5Ti-0.5Fe alloy’s hot-deformed microstructure has more dislocations and finer grains, with Cu_4Ti and Fe_2Ti precipitated phases. The Cu-1.5Ti alloy precipitates the Cu_4Ti phase.

Declaration of competing interest

The authors declare that they have no known competing financial interests or personal relationships that could have appeared to influence the work reported in this paper.

Acknowledgments

This work was supported by the National Natural Science Foundation of China (52071134), the Joint Foundation for Science and Technology Research and Development Plan of Henan Province (232103810030, 232103810031), the Program for Innovative Research Team at the University of the Henan Province (22IRTSTHN001), the China Postdoctoral Science Foundation (2023TQ0107), the Key Research and Development Program of the Jiangxi Province (20224BBE52002).

References

[1] Pang Y, Chao G, Luan T, Gong S, Wang Y, Jiang Z, Xiao Z, Jiang Y, Li Z. Microstructure and properties of high strength, high conductivity and magnetic Cu-10Fe-0.4Si alloy. Mater Sci Eng, A 2021;826. https://doi.org/10.1016/j.msea.2021.142012.

[2] Yang H, Ma Z, Lei C, Meng L, Fang Y, Liu J, Wang H. High strength and high conductivity Cu alloys: a review. Sci China Technol Sci 2020;63(12):2505–17. https://doi.org/10.1007/s11431-020-1633-8.

[3] Wang W, Xiao Z, Lei Q, Meng H, Guo Q, Yang Y, Li Z. A multiphase strengthened Cu-Nb-Si alloy with high strength and high conductivity. Mater Char 2021;182. https://doi.org/10.1016/j.matchar.2021.111565.

[4] Yu J, Wang L, Guan Y, Shao B, Liu Z, Zong Y. A high strength and high electrical conductivity graphene/Cu composite with good high-temperature stability. Mater Char 2023;201. https://doi.org/10.1016/j.matchar.2023.112928.

[5] Yu J, Zhao F, Yang H, Liu J, Ma J, Fang Y. Progress in research on nanoprecipitates in high-strength conductive copper alloys: a review. J Zhejiang Univ - Sci 2023;24(3):206–25. https://doi.org/10.1631/jzus.A2200398.

[6] Zhang X, Zhang Y, Tian B, Song K, Liu P, Jia Y, Chen X, An J, Zhao Z, Liu Y, Volinsky AA, Li X, Yin T. Review of nano-phase effects in high strength and conductivity copper alloys. Nanotechnol Rev 2019;8(1):383–95. https://doi.org/10.1515/ntrev-2019-0034.

[7] Yang K, Wang Y, Guo M, Wang H, Mo Y, Dong X, Lou H. Recent development of advanced precipitation-strengthened Cu alloys with high strength and conductivity: a review. Prog Mater Sci 2023;138. https://doi.org/10.1016/j.pmatsci.2023.101141.

[8] Ban Y, Zhou M, Zhang Y, Jia Y, Pang Y, Li Y, Tang S, Li X, Volinsky AA, Marchenko ES. Abnormally high work hardening ability and excellent comprehensive properties of copper alloys due to multiple twins and precipitates. Mater Des 2023;228. https://doi.org/10.1016/j.matdes.2023.111819.

[9] Wang W, Zhu J, Qin N, Zhang Y, Li S, Xiao Z, Lei Q, Li Z. Effects of minor rare earths on the microstructure and properties of Cu-Cr-Zr alloy. J Alloys Compd 2020;847. https://doi.org/10.1016/j.jallcom.2020.155762.

[10] Liao Y, Guo C, Zhou C, Xie W, Yang B, Wang H. Stability of the metastable β’-Cu4Ti phase in Cu-Ti alloys: role of the Ti content. Mater Char 2023;203. https://doi.org/10.1016/j.matchar.2023.113164.

[11] Wang X, Xiao Z, Qiu W-t, Li Z, Liu F. The evolution of microstructure and properties of a Cu-Ti-Cr-Mg-Si alloy with high strength during the multi-stage thermomechanical treatment. Mater Sci Eng, A 2021;803. https://doi.org/10.1016/j.msea.2020.140510.

[12] Geng G, Wang D, Zhang W, Liu L, Laptev AM. Fabrication of Cu-Ni-Si alloy by melt spinning and its mechanical and electrical properties. Mater Sci Eng, A 2020;776. https://doi.org/10.1016/j.msea.2020.138979.

[13] Wang W, Wang J, Li S, Wang C, Zhou J, Zeng J, Tan W, Wang B. Effects of Nb addition on the properties and microstructure of Cu-Ni-Si-Mg alloy. Mater Char 2022;194. https://doi.org/10.1016/j.matchar.2022.112451.

[14] Yang Y-H, Li S-Y, Cui Z-S, Li Z, Li Y-P, Lei Q. Microstructure and properties of high-strength Cu-Ni-Si-(Ti) alloys. Rare Met 2021;40(11):3251–60. https://doi.org/10.1007/s12598-020-01699-5.

[15] Li L, Kang H, Zhang S, Li R, Yang X, Chen Z, Guo E, Wang T. Microstructure and properties of Cu-Cr-Zr (Mg) alloys subjected to cryorolling and aging treatment. J Alloys Compd 2023;938. https://doi.org/10.1016/j.jallcom.2022.168656.

[16] Ma S, Zhang Q, Fan J, Fu L, Liu M, Shan A. Excellent combination of strength, conductivity and ductility realized in a dilute Cu-Cr-Zr alloy by coherent nanoprecipitates. Mater Sci Eng, A 2023;885. https://doi.org/10.1016/j.msea.2023.145614.

[17] Li J, Ding H, Li B, Li W. Microstructure evolution and properties of a Cu-Cr-Zr alloy with high strength and high conductivity. Mater Sci Eng, A 2021;819. https://doi.org/10.1016/j.msea.2021.141464.

[18] Huang L, Cui Z, Meng X, Zhang X, Zhang X, Song X, Tang N, Xiao Z, Lei Q, Li Z. Effects of microelements on the microstructure evolution and properties of ultrahigh strength Cu-Ti alloys. Mater Sci Eng, A 2021;823. https://doi.org/10.1016/j.msea.2021.141581.

[19] Huang L, Peng L, Mi X, Zhao G, Huang G, Xie H, Zhang W. Relationship between microstructure and properties of high-strength Cu-Ti-Cr alloys during aging. J Alloys Compd 2023;942. https://doi.org/10.1016/j.jallcom.2023.168865.

[20] Li S, Li Z, Xiao Z, Li S, Shen L, Dong Q. Microstructure and property of Cu-2.7Ti-0.15Mg-0.1Ce-0.1Zr alloy treated with a combined aging process. Mater Sci Eng, A 2016;650:345–53. https://doi.org/10.1016/j.msea.2015.10.062.

[21] Rouxel B, Cayron C, Bornand J, Sanders P, Loge RE. Micro-addition of Fe in highly alloyed Cu-Ti alloys to improve both formability and strength. Mater Des 2022;213. https://doi.org/10.1016/j.matdes.2021.110340.

[22] Yang H, Bu Y, Wu J, Fang Y, Liu J, Huang L, Wang H. High strength, high conductivity and good softening resistance Cu-Fe-Ti alloy. J Alloys Compd 2022;925. https://doi.org/10.1016/j.jallcom.2022.166595.

[23] Huang L, Cui Z, Meng X, Li X, Sheng X, Lei Q. Effect of trace alloying elements on the stress relaxation properties of high strength Cu-Ti alloys. Mater Sci Eng, A 2022;846. https://doi.org/10.1016/j.msea.2022.143281.

[24] Wang Y, Song Y, Fan Y, Zhao H, Hong Z, Song K, Dong X, Guo C. Double-peak precipitation hardening in the Cu-Fe-Ti alloy. Scripta Mater 2023;232. https://doi.org/10.1016/j.scriptamat.2023.115478.

[25] Li C, Wang X, Li B, Shi J, Cao Z, Liu Y. Microstructure evolution, mechanical properties and tribological behaviors of copper alloy aged at different temperatures. Vacuum 2021;187. https://doi.org/10.1016/j.vacuum.2021.110156.

[26] Liu J, Wang X, Chen J, Liu J. The effect of cold rolling on age hardening of Cu-3Ti-3Ni-0.5Si alloy. J Alloys Compd 2019;797:370–9. https://doi.org/10.1016/j.jallcom.2019.05.091.

[27] Lebreton V, Pachoutinski D, Bienvenu Y. An investigation of microstructure and mechanical properties in Cu-Ti-Sn alloys rich in copper. Mater Sci Eng, A 2009;508 (1–2):83–92. https://doi.org/10.1016/j.msea.2009.01.050.

[28] Wang X, Chen C, Guo T, Zou J, Yang X. Microstructure and properties of ternary Cu-Ti-Sn alloy. J Mater Eng Perform 2015;24(7):2738–43. https://doi.org/10.1007/s11665-015-1483-4.

[29] Huang K, Loge RE. A review of dynamic recrystallization phenomena in metallic materials. Mater Des 2016;111:548–74. https://doi.org/10.1016/j.matdes.2016.09.012.

[30] Xu D, Zhou M, Zhang Y, Tang S, Zhang Z, Liu Y, Tian B, Li X, Jia Y, Volinsky AA, Li D, Liu Q. Microstructure and hot deformation behavior of the Cu-Sn-Ni-Zn-Ti (-Y) alloy. Mater Char 2023;196. https://doi.org/10.1016/j.matchar.2022.112559.

[31] Song T, Xu SY, Li YL, Ding H. Hot deformation and dynamic recrystallization behavior of a Cu-9Ni-6Sn-0.04Cr alloy. Mater Today Commun 2023;35. https://doi.org/10.1016/j.mtcomm.2023.105828.

[32] Xu DY, Zhou M, Zhang Y, Tang SL, Zhang ZY, Liu Y, Tian BH, Li X, Jia YL, Volinsky AA, Li D, Liu QJ. Microstructure and hot deformation behavior of the Cu-Sn-Ni-Zn-Ti (-Y) alloy. Mater Char 2023;196. https://doi.org/10.1016/j.matchar.2022.112559.

[33] Shen Z, Lin ZZ, Shi PJ, Tang GP, Zheng TX, Liu CM, Guo YF, Zhong YB. Enhanced strength, ductility and electrical conductivity of Cu-Te alloys via dynamic recrystallization and precipitation. Mater Sci Eng, A 2021;820. https://doi.org/10.1016/j.msea.2021.141548.

[34] Wang QJ, Ren XL, Wang L, Yan TR, Wang KS, Xu BF. Study on hot deformation behavior and dynamic recrystallization mechanism of Cu-Ti-Fe alloy. Adv Eng Mater 2023. https://doi.org/10.1002/adem.202301618.

[35] Zhao C, Wang Z, Pan DQ, Li DX, Luo ZQ, Zhang DT, Yang C, Zhang WW. Effect of Si and Ti on dynamic recrystallization of high-performance Cu-15Ni-8Sn alloy during hot deformation. Trans Nonferrous Metals Soc China 2019;29(12):2556–65. https://doi.org/10.1016/s1003-6326(19)65163-0.

[36] Sellars C, McTegart WJJAM. On the mechanism of hot deformation, vol. 14; 1966. p. 1136–8.

[37] Wang X, Li Z, Xiao Z, Qiu W-t. Microstructure evolution and hot deformation behavior of Cu-3Ti-0.1Zr alloy with ultra-high strength. Trans Nonferrous Metals Soc China 2020;30(10):2737–48. https://doi.org/10.1016/s1003-6326(20)65416-4.

[38] Liu J, Wang X, Liu J, Liu Y, Li H, Wang C. Hot deformation and dynamic recrystallization behavior of Cu-3Ti-3Ni-0.5Si alloy. J Alloys Compd 2019;782: 224–34. https://doi.org/10.1016/j.jallcom.2018.12.212.

[39] Geng Y, Zhang Y, Song K, Jia Y, Li X, Stock H-R, Zhou H, Tian B, Liu Y, Volinsky AA, Zhang X, Liu P, Chen X. Effect of Ce addition on microstructure evolution and precipitation in Cu-Co-Si-Ti alloy during hot deformation. J Alloys Compd 2020;842. https://doi.org/10.1016/j.jallcom.2020.155666.

[40] Wu Y, Qin X, Wang C, Zhou L. Influence of phosphorus on hot deformation microstructure of a Ni-Fe-Cr based alloy. Mater Sci Eng, A 2019;768. https://doi.org/10.1016/j.msea.2019.138454.

[41] Ban Y, Zhang Y, Tian B, Song K, Zhou M, Zhang X, Jia Y, Li X, Geng Y, Liu Y, Volinsky AA. EBSD analysis of hot deformation behavior of Cu-Ni-Co-Si-Cr alloy. Mater Char 2020;169. https://doi.org/10.1016/j.matchar.2020.110656.

[42] Liu P, Zhang R, Yuan Y, Cui C, Zhou Y, Sun X. Hot deformation behavior and workability of a Ni-Co based superalloy. J Alloys Compd 2020;831. https://doi.org/10.1016/j.jallcom.2020.154618.

[43] Yu H, Wang D, Liu Y, Liu Y, Huang L, Jiang B, Park S, Yu W, Yin F. Recrystallization mechanisms and texture evolution of AZ31 alloy by gradient caliber rolling. J Mater Res Technol JMR&T 2023;23:611–26. https://doi.org/10.1016/j.jmrt.2023.01.044.

[44] Xin Ga, Zhou M, Jing K, Hu H, Li Za, Zhang Y, Bai Q, Tian C, Tian B, Li X, Volinsky AA, Zou J. Heat treatment effects on microstructure and properties of Cu–Ti–Fe alloys. Mater Sci Eng, A 2024;892:146068. https://doi.org/10.1016/j.msea.2023.146068.